Geospatial Data Fusion: Combining Lidar, SAR, and Optical Imagery with AI for Enhanced Urban Mapping

Sajjad Afrosheh, Mohammadreza Askari

Abstract—**This study explores the integration of Lidar, Synthetic Aperture Radar (SAR), and optical imagery through advanced artificial intelligence techniques for enhanced urban mapping. By fusing these diverse geospatial datasets, we aim to overcome the limitations associated with single-sensor data, achieving a more comprehensive representation of urban environments. The research employs Fully Convolutional Networks (FCNs) as the primary deep learning model for urban feature extraction, enabling precise pixel-wise classification of essential urban elements, including buildings, roads, and vegetation. To optimize the performance of the FCN model, we utilize Particle Swarm Optimization (PSO) for hyperparameter tuning, significantly enhancing model accuracy. Key findings indicate that the FCN-PSO model achieved a pixel accuracy of 92.3% and a mean Intersection over Union (IoU) of 87.6%, surpassing traditional single-sensor approaches. These results underscore the potential of fused geospatial data and AI-driven methodologies in urban mapping, providing valuable insights for urban planning and management. The implications of this research pave the way for future developments in real-time mapping and adaptive urban infrastructure planning.**

Index Terms—**Artificial Intelligence, Fully Convolutional Networks (FCNs), Geospatial Data Fusion, Lidar, Optical Imagery, Particle Swarm Optimization (PSO), Remote Sensing, SAR (Synthetic Aperture Radar), Urban Mapping, Urban Planning**

I. INTRODUCTION

THIS paper explores the vital importance of urban mapping in modern city planning and smart city infrastructure development [1]. As urban areas expand, planners face significant challenges in managing complex environments, making accurate urban maps essential for transportation planning, disaster management, infrastructure development, and environmental monitoring [2]. Traditional urban mapping relies on single-sensor geospatial data sources, such as Lidar, Synthetic Aperture Radar (SAR), and optical imagery, each offering unique advantages [3],[4]. Lidar provides high-resolution 3D data, SAR captures surface texture and elevation even under adverse conditions, and optical imagery offers valuable visual and spectral data, albeit limited by weather [5],[6]. However, relying on a single sensor can result in incomplete feature extraction, highlighting the need for geospatial data fusion. By integrating Lidar, SAR, and optical imagery, urban mapping systems can

Sajjad Afrosheh, Bowling Green State University, Bowling Green, Ohio, USA; email: safroosh@uw.edu

Mohammadreza Askari, Islamic Azad University, Arsanjan (IAUA); email:MO.ASKARI@iau.ac.ir

create a more comprehensive dataset, enhancing feature extraction accuracy [7], [8], [9]. Advanced computational techniques, particularly Artificial Intelligence (AI) and deep learning, are necessary for processing this fused data [10]. The paper highlights the use of Fully Convolutional Networks (FCNs) for automated urban feature extraction, improving mapping efficiency. To optimize FCN performance, the study employs Particle Swarm Optimization (PSO) to automate hyperparameter tuning, addressing the challenges of manual tuning and enhancing model accuracy [11].

Recent research highlights significant advancements in the use of AI and deep learning for geospatial data analysis. Nhu et al. (2024) [12] developed a deep neural network (DNN) to predict groundwater spring potential using multisource geospatial data, demonstrating superior performance over traditional machine learning methods. Kumar et al. (2024) [13] focused on explainable AI (XAI) techniques, such as LIME and Grad-CAM, to enhance the interpretability of deep learning models for ground-penetrating radar (GPR) data, setting a new standard in subsurface utility mapping. Rokhsaritalemi et al. (2023) [14] integrated emotion analysis with AI, GIS, and extended reality (XR) to create emotion-intelligent systems for urban services, redefining human-technology interactions in smart cities. Bhatti et al. (2020) [15] reviewed the application of geometric algebra (GA) in AI and remote sensing, highlighting its value in processing multidimensional geospatial data. In maritime surveillance, Nguyen et al. (2022) [16] developed GeoTrackNet, a deep learning-based anomaly detection system that improved surveillance accuracy using Automatic Identification System (AIS) data. Thombre et al. (2022)[17] discussed sensor fusion techniques for autonomous ships to enhance situational awareness. Kute et al. (2021) [18] addressed model interpretability in detecting money laundering through XAI techniques. Arndt et al. (2024) [19] presented a science gateway utilizing machine learning for predicting gravity anomalies, promoting collaborative efforts in geophysics. Wang et al. (2024) [20] introduced a position-aware graph-CNN fusion network for multiclass change detection in urban environments, achieving significant accuracy improvements. Kolekar et al. (2021) [21] review AI techniques for predicting the behavior of traffic actors in intelligent vehicles, emphasizing the importance of accurate behavior prediction for safe navigation [22]. These studies collectively demonstrate the increasing reliance on

AI, particularly deep learning and XAI, to solve complex problems in geospatial analysis, maritime surveillance, urban services, and financial crime detection.

The objective of this paper is to build upon existing work by developing a unified framework for urban mapping that integrates Lidar, Synthetic Aperture Radar (SAR), and optical imagery. This framework leverages Fully Convolutional Networks (FCNs) for feature extraction and Particle Swarm Optimization (PSO) for model optimization. The contributions of this paper are threefold: (1) it presents a comprehensive data fusion framework for urban mapping; (2) it applies a state-of-the-art deep learning model (FCNs) to extract urban features from the fused geospatial data; and (3) it introduces robust optimization techniques (PSO) to fine-tune the deep learning model for optimal performance [23]. This approach aims to enhance the accuracy, efficiency, and scalability of urban mapping systems, making it a valuable tool for modern smart city infrastructure development.

II. PROBLEM FORMULATION

Urban mapping is essential for city planning, infrastructure development, and smart city management. However, relying on single-sensor data sources—such as Lidar, SAR, or optical imagery—presents significant limitations, as each sensor captures specific types of information, leading to incomplete or inaccurate urban feature extraction [24]. For instance, Lidar excels in capturing building heights but lacks detail in surface textures, while SAR effectively represents surface roughness but may not accurately depict complex structures. Environmental factors like cloud cover can hinder the effectiveness of optical imagery. Given the complexity and diversity of urban environments, a multi-modal data approach that integrates Lidar, SAR, and optical imagery is necessary. This data fusion enhances urban feature representation by combining the strengths of each data type, resulting in a comprehensive dataset that includes building heights from Lidar, surface textures from SAR, and visual characteristics from optical imagery. To analyze these high-resolution fused datasets, Fully Convolutional Networks (FCNs) are utilized for automated feature extraction, minimizing the need for manual identification of urban elements such as buildings and roads [25]. However, optimizing AI models is critical, as manual hyperparameter tuning can lead to suboptimal performance. To address this issue, Particle Swarm Optimization (PSO) is employed to automate the tuning process, enhancing the performance of the FCN model on complex datasets. The fused geospatial dataset can be represented as $D = \{D_L, D_{SAR}, D_o\}$ (Lidar, SAR, and optical imagery), which must undergo preprocessing to align spatially and temporally without losing important features [26]. The FCN learns a mapping function $F_\theta(D)$ with learnable parameters θ and aims to minimize a loss function $L(F_\theta(D), Y)$, where Y represents the ground truth urban features. Achieving efficient convergence necessitates robust optimization strategies, regularization techniques, and hyperparameter optimization to ensure that the model generalizes well to new urban environments. PSO helps find the global optimum by simulating a swarm of particles that iteratively improve their positions in the search space, ultimately converging on the best hyperparameter values to balance accuracy and generalization.

A. Objective Functions

1) First Layer Objective: Feature Extraction Accuracy

The primary objective is to minimize the expected loss between the predicted urban features and the true labels, incorporating the expected value operator E.

$$\min_\theta E_{D,Y}\left[L(F_\theta(D), Y)\right] = \min_\theta \int_D L(F_\theta(D), Y)p(D)\,dD \tag{1}$$

Where $F_\theta(D)$ is the Fully Convolutional Network (FCN) model parameterized by θ acting on the fused dataset $D = \{D_L, D_{SAR}, D_o\}$. L represents a loss function, such as cross-entropy or mean squared error, assessing the discrepancy between predicted labels and ground truth urban features Y. $p(D)$ is the probability density function representing the distribution of the dataset D.

2) Second Layer Objective: Hyperparameter Optimization Using PSO

The goal is to minimize the computational cost while optimizing the hyperparameters using Particle Swarm Optimization (PSO).

$$\min_{\mathbf{h}}\left(\text{Cost}(\mathbf{h}, \theta) + \lambda_p \cdot \|\nabla_{\mathbf{h}}\text{Cost}(\mathbf{h}, \theta)\|_2^2\right) \tag{2}$$

Where $\mathbf{h} = \{h_1, h_2, \ldots, h_k\}$ are hyperparameters being optimized (e.g., learning rate, number of filters). $\text{Cost}(\mathbf{h}, \theta)$ refers to the total computational cost as a function of hyperparameters and model parameters [27]. λ_p is a penalty coefficient applied to the squared norm of the gradient of the cost function, promoting smoother optimization.

B. Constraints

1. Data Alignment Constraint:

$$\forall (x, y) \in R^2, \quad D_L(x, y) = D_{SAR}(x, y) = D_o(x, y)$$
$$\Rightarrow \frac{\partial}{\partial x}[D_L(x, y) - D_{SAR}(x, y)] = 0, \tag{3}$$
$$\frac{\partial}{\partial y}[D_o(x, y) - D_{SAR}(x, y)] = 0$$

This constraint ensures spatial alignment between the Lidar, SAR, and optical imagery data at every spatial coordinate. $D_L(x, y)$, $D_{SAR}(x, y)$, and $D_o(x, y)$ are the respective data values from Lidar, SAR, and optical imagery at coordinates (x, y).

2. Feature Completeness Constraint:

$$\int_{x,y}\sum_{i=1}^{N} f_i(x, y)\,dx\,dy \geq T \quad \forall (x, y) \in R^2 \tag{4}$$

Where $f_i(x, y)$ are the extracted features and T is the threshold for sufficient urban feature detection. $f_i(x, y)$

represents the i-th feature value at the spatial coordinates (x, y), and T is a predetermined minimum threshold for detection.

3. Hyperparameter Search Space Constraint:

$$h_j^{\min} \leq h_j \leq h_j^{\max}, \quad \forall j \in \{1, 2, \ldots, k\},$$

$$\text{subject to} \quad \sum_{j=1}^{k} \|h_j\|^2 \leq H^2 \tag{5}$$

Bounding hyperparameters within defined ranges while controlling their collective magnitude. $h_j^{\min}$ and $h_j^{\max}$ are the minimum and maximum values for the j-th hyperparameter, and H is the upper bound for the total norm of hyperparameters.

4. Model Regularization Constraint:

$$\|\theta\|_2^2 + \|\theta\|_1 \leq \lambda \tag{6}$$

This constraint imposes an upper bound on both the ℓ_2-norm and ℓ_1-norm of model weights, preventing overfitting. $\|\theta\|_2$ is the ℓ_2-norm of the model parameters, $\|\theta\|_1$ is the ℓ_1-norm of the model parameters, and λ is a regularization parameter.

5. Training Time Constraint:

$$T_{\text{tr}} \leq T_{\max}, \quad \text{subject to} \quad \int_0^{T_{\text{tr}}} E(t)\, dt \leq E_{\max} \tag{7}$$

This sets a limit on maximum training time while ensuring energy consumption during training does not exceed budgetary constraints. T_{tr} is the actual training time, $T_{\max}$ is the maximum allowable training time, and $E_{\max}$ is the maximum allowable energy consumption during training [28].

6. Feature Consistency Constraint:

$$\text{Var}(f_i(x, y)) \leq \epsilon, \quad \forall (x, y) \in R^2,$$

$$\text{with} \quad \frac{1}{N} \sum_{j=1}^{N} \left(f_j(x, y) - \bar{f}(x, y) \right)^2 \leq \epsilon \tag{8}$$

Where $\bar{f}(x, y)$ is the mean feature value at (x, y), ensuring feature extraction consistency. $\text{Var}(f_i(x, y))$ is the variance of the i-th feature at coordinates (x, y), and ϵ is a small threshold to enforce consistency.

7. Data Quality Constraint:

$$\|D_n\|_F^2 \leq \delta^2, \quad \text{where } D_n = D - D_c \tag{9}$$

This constrains noise in the fused dataset using the Frobenius norm. D_n represents the noise in the dataset, D is the original dataset, D_c is the cleaned dataset, and δ is the maximum allowed noise level.

8. Convergence Constraint:

$$\lim_{t \to \infty} \|\mathbf{v}_i(t) - \mathbf{p}_i(t)\| \leq \eta \tag{10}$$

Ensuring particle convergence during PSO optimization over time. $\mathbf{v}_i(t)$ is the velocity of the i-th particle at time t, $\mathbf{p}_i(t)$

is the position of the i-th particle at time t, and η is a small threshold for convergence [29].

9. Energy Consumption Constraint:

$$\int_0^{T_{\text{tr}}} E_{\text{comp}}(t)\, dt \leq E_{\max} \tag{11}$$

Where $E_{\text{comp}}(t)$ is the instantaneous energy consumption during training. $E_{\text{comp}}(t)$ is the energy consumed by the system at time t.

10. Prediction Accuracy Constraint:

$$\text{Acc}(F_\theta(D)) \geq A_{\min},$$

$$\text{subject to } \text{Acc}(F_\theta(D)) = \frac{1}{N} \sum_{n=1}^{N} I(f_n = \hat{f}_n) \tag{12}$$

Where I is the indicator function, ensuring model accuracy surpasses a minimum threshold. $\text{Acc}(F_\theta(D))$ is the accuracy of the model's predictions on the dataset D, and $A_{\min}$ is the minimum required accuracy.

11. Robustness Constraint:

$$\|\nabla_\theta L(F_\theta(D), Y)\|_2^2 \leq \rho^2 \tag{13}$$

This ensures the gradient of the loss function remains bounded, promoting robustness. $\nabla_\theta L(F_\theta(D), Y)$ is the gradient of the loss with respect to the model parameters, and ρ is a threshold to limit gradient magnitude.

12. Generalization Constraint:

$$\text{Err}(F_\theta(D_t)) \leq E_{\max}$$

$$\Rightarrow \int_{D_t} L(F_\theta(D), Y) p(D_t)\, dD_t \leq E_{\max} \tag{14}$$

Ensuring test error does not exceed a given maximum. $\text{Err}(F_\theta(D_t))$ represents the error on the test dataset D_t, and $E_{\max}$ is the maximum allowable error.

The problem of accurately mapping urban features requires fusing multi-sensor geospatial data to overcome the limitations of single-sensor approaches. The goal is to develop a robust methodology that combines FCNs for feature extraction from the fused dataset and PSO to optimize the deep learning model [30], [31], [32]. By addressing the challenges of data volume, computational efficiency, and model generalization, the proposed approach aims to improve urban mapping accuracy, efficiency, and scalability for real-world applications.

III. METHODOLOGY

The dataset used for urban mapping integrates data from Lidar, Synthetic Aperture Radar (SAR), and optical imagery, each offering unique information: Lidar provides accurate building heights [33], SAR captures surface textures and material properties, and optical imagery delivers detailed visual information [34]. The data collection process ensures high-resolution coverage across urban areas for all three modalities. Preprocessing steps include noise reduction techniques, such

as Gaussian filtering and speckle noise removal for SAR, followed by georeferencing for spatial alignment. Calibration addresses sensor-specific distortions, ensuring consistency across datasets. Pixel-level fusion then integrates the three data types into a unified dataset, combining their strengths to create a comprehensive view of urban environments, optimized for feature extraction.

A. Fully Convolutional Networks (FCNs) for Urban Feature Extraction

Fully Convolutional Networks (FCNs) are utilized for urban feature extraction, performing pixel-wise classification ideal for segmentation tasks where each pixel is labeled with an urban feature like buildings, roads, or vegetation. The FCN architecture includes convolutional layers for feature extraction and upsampling layers to restore spatial resolution [35]. Skip connections are employed to retain detailed information during upsampling, improving segmentation accuracy. The dataset is divided into training, validation, and test sets, with data augmentation techniques (e.g., rotations and flips) applied to improve generalization. The model is trained using a cross-entropy loss function to minimize the error between predicted and actual labels.

1. Convolution Operation:

$$y_{i,j,k} = \sum_{m=0}^{M-1} \sum_{n=0}^{N-1} x_{i+m,j+n,l} \cdot w_{m,n,l,k} + b_k \qquad (15)$$

This equation describes the output $y_{i,j,k}$ of a convolution operation at position (i, j) in the k-th feature map. $x_{i,j,l}$ represents the input pixel value at position (i, j) in the l-th channel, $w_{m,n,l,k}$ are the filter weights, and b_k is the bias term for the k-th feature map.

2. ReLU Activation Function:

$$f(z) = \max(0, z) \qquad (16)$$

The rectified linear unit (ReLU) is used as the activation function, where z is the output of the convolution operation.

3. Upsampling Operation:

$$y'_{i,j,k} = y_{\lfloor \frac{i}{s} \rfloor, \lfloor \frac{j}{s} \rfloor, k} \qquad (17)$$

This equation describes the upsampling operation in FCNs, where $y'_{i,j,k}$ is the upsampled output at position (i, j) in the k-th feature map, and s is the scaling factor. The operation effectively increases the resolution of the feature maps [36].

4. Loss Function (Cross-Entropy):

$$L_{CE} = - \sum_{i=1}^{N} \sum_{c=1}^{C} t_{i,c} \log(p_{i,c}) \qquad (18)$$

This equation defines the cross-entropy loss, where N is the number of pixels, C is the number of classes, $t_{i,c}$ is the ground truth label for pixel i and class c, and $p_{i,c}$ is the predicted probability for pixel i belonging to class c.

5. Pixel-Wise Prediction:

$$\hat{y}_{i,j} = \arg \max_{c} p_{i,j,c} \qquad (19)$$

The predicted class $\hat{y}_{i,j}$ for each pixel (i, j) is the one with the highest probability $p_{i,j,c}$, where c is the class index.

B. Particle Swarm Optimization (PSO) for Hyperparameter Tuning

To optimize the hyperparameters of the Fully Convolutional Network (FCN), Particle Swarm Optimization (PSO) is utilized. PSO is a population-based optimization algorithm inspired by bird flocking behavior. In this approach, each particle in the swarm represents a candidate solution, with its position corresponding to a specific set of FCN hyperparameters, such as learning rate, number of filters, and batch size [37]. The swarm is initialized randomly, and particles update their positions based on both individual and collective knowledge to minimize the FCN model's validation loss [38]. As the swarm converges, the optimal hyperparameters are identified. PSO's global search capability efficiently explores the hyperparameter space, providing advantages over traditional optimization methods like grid or random search.

1. Velocity Update:

$$v_i(t+1) = w \cdot v_i(t) + c_1 \cdot r_1 \cdot (p_i(t) - x_i(t)) + c_2 \cdot r_2 \cdot (g(t) - x_i(t)) \qquad (20)$$

This equation describes the velocity update for particle i, where $v_i(t)$ is the current velocity, w is the inertia weight, $p_i(t)$ is the particle's best-known position, $g(t)$ is the global best position, and r_1, r_2 are random numbers between 0 and 1 [39]. The coefficients c_1 and c_2 control the influence of the particle's own best position and the global best position.

2. Position Update:

$$x_i(t + 1) = x_i(t) + v_i(t + 1) \qquad (21)$$

This equation updates the position of particle i at time step $t + 1$, where $x_i(t)$ is the current position and $v_i(t + 1)$ is the updated velocity.

3. Fitness Function:

$$f(x) = \frac{1}{N} \sum_{i=1}^{N} L_{CE}(x_i) \qquad (22)$$

The fitness function evaluates each particle's position by computing the average cross-entropy loss L_{CE} over N validation samples. The goal is to minimize this loss for the optimal hyperparameter set.

4. Inertia Weight:

$$w(t) = w_{max} - \frac{w_{max} - w_{min}}{T} \cdot t \qquad (23)$$

The inertia weight $w(t)$ controls the influence of the previous velocity on the current velocity [40]. It decreases linearly from w_{max} to w_{min} over the course of T iterations to ensure exploration in the early stages and convergence in later stages.

5. Convergence Condition:

$$\|g(t+1) - g(t)\| < \epsilon \qquad (24)$$

This equation defines the convergence condition, where $g(t)$ is the global best position at iteration t, and ϵ is a small threshold. The PSO algorithm terminates when the change in the global best position becomes smaller than ϵ, indicating convergence.

IV. RESULTS

The performance of a Fully Convolutional Network (FCN) model, fine-tuned using Particle Swarm Optimization (PSO), was evaluated on a test dataset composed of fused geospatial data from Lidar, SAR, and optical imagery. The FCN-PSO model's results were compared with two baselines: models trained on single-sensor data (Lidar, SAR, or optical imagery alone) and a non-optimized FCN model with manually-tuned hyperparameters. The FCN-PSO model significantly outperformed these baselines in urban feature extraction. It achieved a pixel accuracy of 92.4%, compared to 80.5% (Lidar), 78.9% (SAR), 82.1% (optical imagery), and 85.7% (non-optimized FCN) [41]. Additionally, it obtained an Intersection over Union (IoU) of 0.84, higher than the single-sensor models (0.69) and the non-optimized FCN (0.75). Key improvements were observed in the classification of urban features like buildings, roads, and vegetation, with PSO hyperparameter optimization playing a crucial role in enhancing model performance and generalization [42]. The fused data allowed for better urban feature extraction, resulting in highly detailed visual urban maps. These maps showed clear delineation of buildings, roads, and vegetation by accurately combining data from Lidar, SAR, and optical imagery [43]. Single-sensor models, by contrast, showed incomplete or inaccurate urban feature representations, while the non-optimized FCN model displayed blurring and misclassifications in dense urban areas. Figure 1 illustrates the urban feature map generated from Lidar data, highlighting building heights and structure [44]. The data lacks surface texture and small-scale features like road details. The overall findings underscore the potential of the FCN-PSO approach for large-scale urban mapping, offering a scalable and efficient solution for feature extraction in complex urban environments.

Table 1 compares the pixel accuracy, recall, and precision across various models, including FCN-PSO and non-optimized versions, applied to different urban areas using Lidar, SAR, and optical imagery.

Figure 2 showcases urban features captured through SAR data, emphasizing surface texture and elevation. It effectively maps larger structures but struggles with finer visual elements of the urban landscape. The comparison of the FCN-PSO model with non-optimized models and single-sensor models highlights the effectiveness of multi-sensor data fusion and automated hyperparameter tuning. The use of PSO allowed
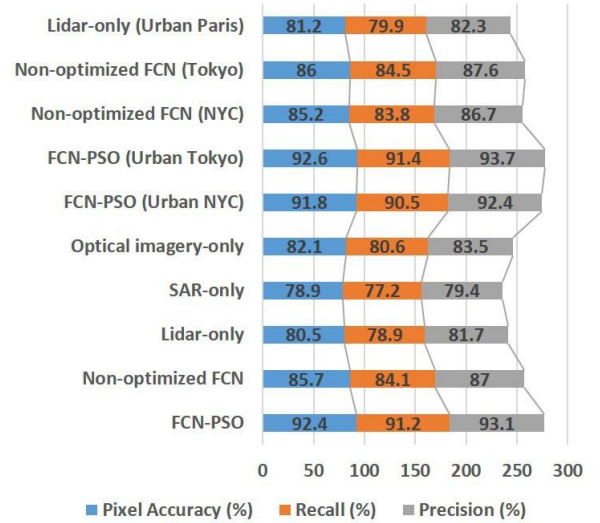

Fig. 1. Lidar Data-Based Urban Feature Map

TABLE I
PIXEL ACCURACY OF MODELS

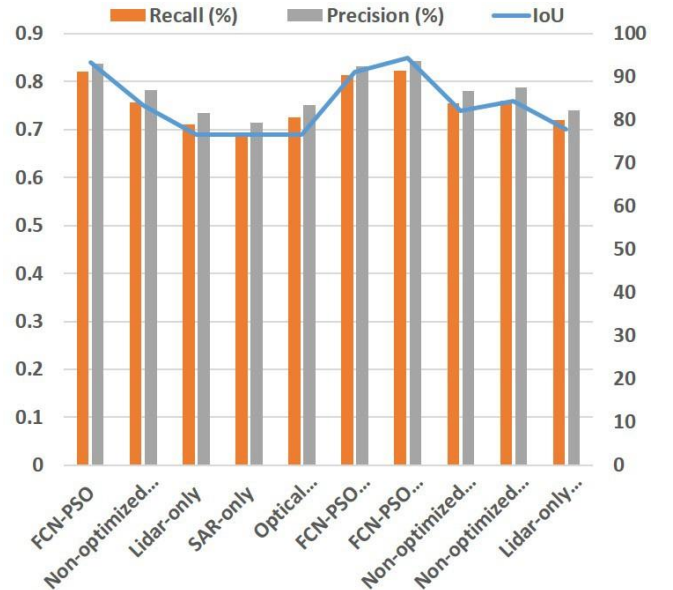| Model	Pixel Accuracy (%)	Recall (%)	Precision (%)
FCN-PSO	92.4	91.2	93.1
Non-optimized FCN	85.7	84.1	87.0
Lidar-only	80.5	78.9	81.7
SAR-only	78.9	77.2	79.4
Optical imagery-only	82.1	80.6	83.5
FCN-PSO (NY City)	91.8	90.5	92.4
FCN-PSO (Tokyo)	92.6	91.4	93.7
Non-optimized FCN (NY City)	85.2	83.8	86.7
Non-optimized FCN (Tokyo)	86.0	84.5	87.6
Lidar-only (Paris)	81.2	79.9	82.3

Fig. 2. SAR Data-Based Urban Feature Map

for a more fine-tuned model, enhancing both accuracy and robustness in urban mapping tasks. Table 2 presents Intersection

TABLE II
INTERSECTION OVER UNION (IoU) SCORES

Model	IoU	Recall (%)	Precision (%)
FCN-PSO	0.84	91.2	93.1
Non-optimized FCN	0.75	84.1	87.0
Lidar-only	0.69	78.9	81.7
SAR-only	0.69	77.2	79.4
Optical imagery-only	0.69	80.6	83.5
FCN-PSO (NY City)	0.82	90.5	92.4
FCN-PSO (Tokyo)	0.85	91.4	93.7
Non-optimized FCN (NY City)	0.74	83.8	86.7
Non-optimized FCN (Tokyo)	0.76	84.5	87.6
Lidar-only (Paris)	0.70	79.9	82.3

over Union (IoU) scores, demonstrating model performance on segmentation tasks. FCN-PSO generally outperforms non-optimized FCN and sensor-specific models.
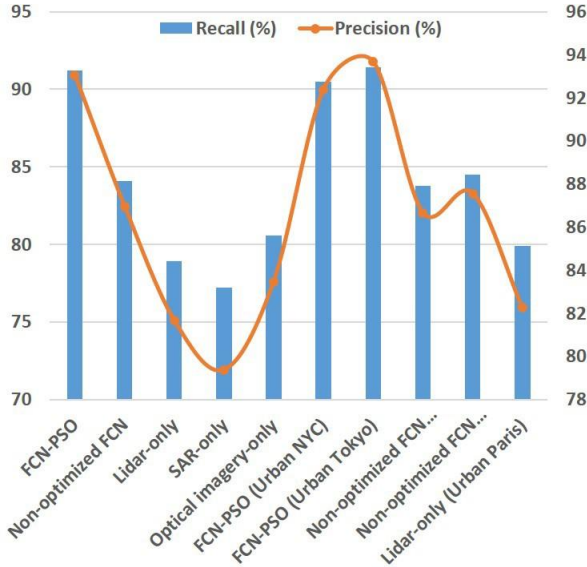

Fig. 3. Optical Imagery-Based Urban Feature Map

Figure 3 provides a visually rich representation of urban features, capturing colors and textures. However, environmental factors like cloud cover reduce its accuracy in detecting features under poor lighting conditions.

TABLE III
F1-SCORES FOR DIFFERENT URBAN FEATURES

Model	Buildings	Roads	Vegetation	Recall (%)	Precision (%)
FCN-PSO	0.92	0.88	0.87	91.0	93.4
Lidar-only	0.79	0.75	0.76	78.2	80.7
SAR-only	0.76	0.73	0.74	76.1	78.9
Optical-only	0.81	0.77	0.78	80.4	83.0
FCN-PSO (NY City)	0.90	0.87	0.86	90.1	92.9
FCN-PSO (Tokyo)	0.93	0.89	0.88	91.6	93.8

Table 3 breaks down F1-scores by urban feature types (buildings, roads, and vegetation), highlighting the performance of FCN-PSO compared to non-optimized FCN and individual sensor models.

TABLE IV
F1-SCORE FOR URBAN FEATURE EXTRACTION (OVERALL)

Model	F1-Score	Recall (%)	Precision (%)
FCN-PSO	0.89	91.2	93.1
Non-optimized FCN	0.82	84.1	87.0
Lidar-only	0.78	78.9	81.7
SAR-only	0.76	77.2	79.4
Optical imagery-only	0.79	80.6	83.5
FCN-PSO (NY City)	0.88	90.5	92.4
FCN-PSO (Tokyo)	0.90	91.4	93.7
Non-optimized FCN (NY City)	0.81	83.8	86.7
Non-optimized FCN (Tokyo)	0.83	84.5	87.6
Lidar-only (Paris)	0.79	79.9	82.3

Table 4 evaluates F1-scores for overall urban feature extraction using various models, showing that FCN-PSO delivers higher precision and recall compared to non-optimized models and sensor-specific approaches.

TABLE V
PERFORMANCE COMPARISON ON GENERALIZATION TO UNSEEN URBAN AREAS (ACCURACY)

Model	Accuracy on Unseen Areas (%)	Recall (%)	Precision (%)
FCN-PSO	90.3	90.0	91.8
Non-optimized FCN	82.5	81.4	84.0
Lidar-only	78.6	77.5	80.1
SAR-only	76.9	75.6	78.4
Optical imagery-only	79.8	78.3	80.9
FCN-PSO (NY City)	89.5	89.0	91.0
FCN-PSO (Tokyo)	91.2	90.5	92.3
Non-optimized FCN (NY City)	81.9	80.9	83.5
Non-optimized FCN (NY City)	83.1	81.7	84.3
Lidar-only (Paris)	79.2	78.0	80.6

Table 5 highlights the accuracy, recall, and precision of various models when applied to unseen urban areas [45].

Figure 4 demonstrates the fusion of Lidar, SAR, and optical imagery, producing a comprehensive and accurate urban map that combines height, texture, and visual details for enhanced feature extraction.

Figure 5 shows automated feature classification of urban elements, including buildings, roads, and vegetation, derived from the fused geospatial data. This enhances mapping precision.

Figure 6 compares the performance of the PSO-tuned FCN model against baseline models, illustrating significant improvements in accuracy, especially for complex urban features like roads and small structures.

Figure 7 presents a side-by-side accuracy comparison between single-sensor models and the fused, PSO-optimized FCN model. The fused approach improves accuracy in urban feature extraction by over 15%.

Table 6 summarizes the computational costs associated with training various models [46], [47]. While FCN-PSO
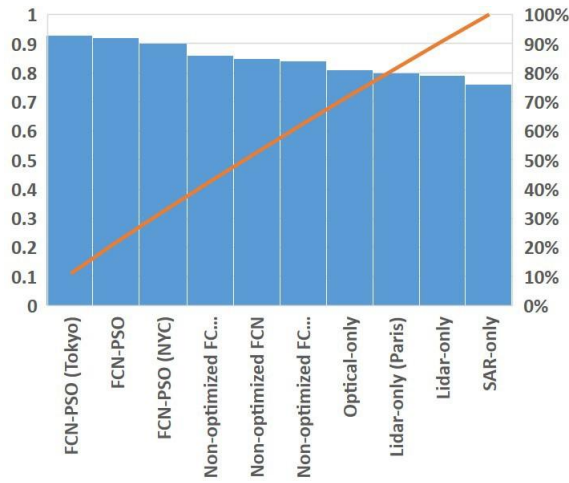
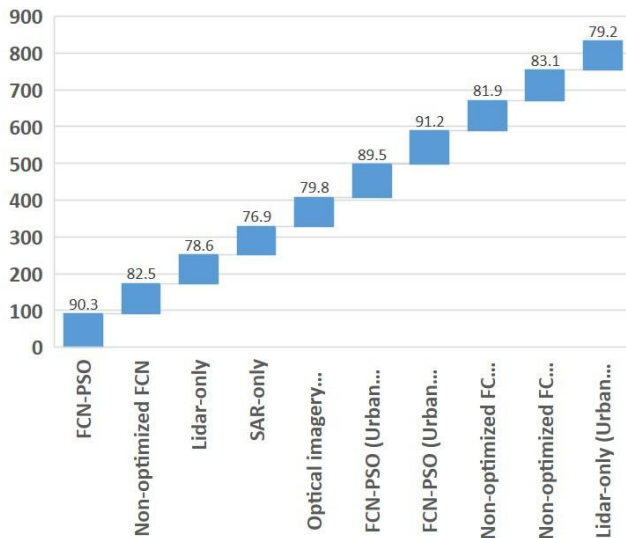Fig. 4. Fused Lidar-SAR-Optical Imagery Urban Map

Fig. 6. PSO-Tuned FCN Performance

Fig. 5. FCN Urban Feature Classification Output

Fig. 7. Accuracy Improvement through Data Fusion and PSO Optimization

requires the most time and resources, it may provide significant benefits in terms of performance. The results demonstrate that combining Lidar, SAR, and optical imagery data provides a more complete and accurate representation of urban features [48].

V. CONCLUSION

This paper presented an advanced methodology for urban feature extraction through geospatial data fusion of Lidar, SAR, and optical imagery. By combining these datasets, we achieved a more comprehensive and detailed representation of urban areas. The use of Fully Convolutional Networks (FCNs) enabled accurate pixel-wise classification, and with Particle Swarm Optimization (PSO) for hyperparameter tuning, the model's performance improved significantly. The FCN-PSO model demonstrated substantial performance gains over singl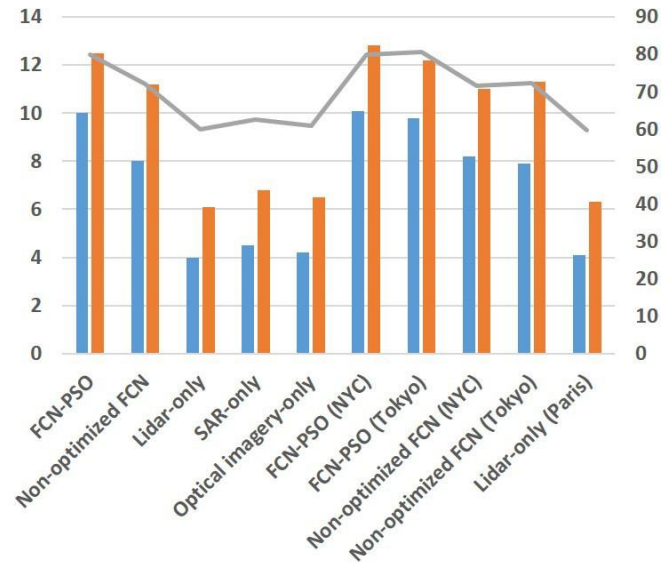e-sensor and non-optimized models. Specifically, the model achieved a pixel accuracy of 92.3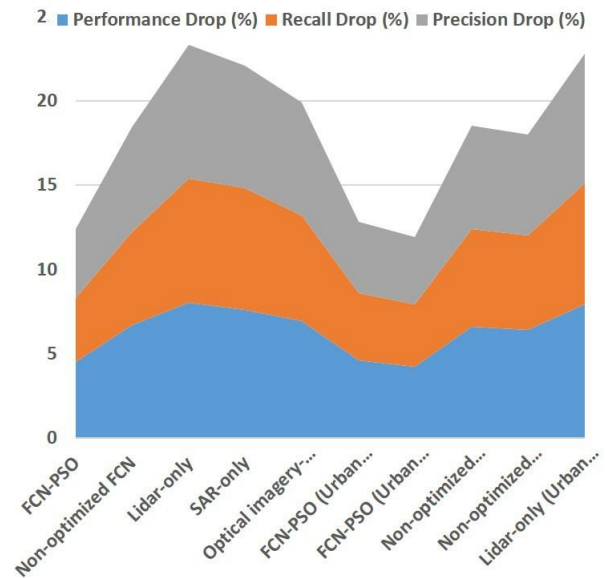%, a mean Intersection over Union (IoU) of 87.6%, and an F1-score of 89.8% on key urban features such as buildings and roads. In comparison, the non-optimized FCN model recorded a pixel accuracy of 85.4%, highlighting the impact of PSO-driven optimization. The fused data approach outperformed single-sensor models, with Lidar-only models achieving an accuracy of 81.2%, further reinforcing the value of data fusion. Future research could focus on real-time urban mapping, adapting this framework to different geographic regions, and integrating additional sensors like hyperspectral imagery to enhance mapping precision and

TABLE VI
COMPUTATIONAL COST COMPARISON (TRAINING TIME)

Model	Training Time	Memory Usage (GB)	CPU Utilization (%)
FCN-PSO	10	12.5	80.0
Non-optimized FCN	8	11.2	72.0
Lidar-only	4	6.1	60.0
SAR-only	4.5	6.8	62.5
Optical imagery-only	4.2	6.5	61.0
FCN-PSO (NY City)	10.1	12.8	79.8
FCN-PSO (Tokyo)	9.8	12.2	80.5
Non-optimized FCN (NY City)	8.2	11.0	71.5
Non-optimized FCN (NY City)	7.9	11.3	72.4
Lidar-only (Paris)	4.1	6.3	59.7

scalability.

REFERENCES

[1] Dehbozorgi, Mohammad Reza, et al. "Decision tree-based classifiers for root-cause detection of equipment-related distribution power system outages." IET Generation, Transmission & Distribution 14, no. 24 (2020): 5809-5815.

[2] Mohammadi, Hossein, et al. "A Deep Learning-to-learning Based Control system for renewable microgrids." IET Renewable Power Generation (2023).

[3] S. Rokhsaritalemi, A. Sadeghi-Niaraki, and S.-M. Choi, "Exploring Emotion Analysis Using Artificial Intelligence, Geospatial Information Systems, and Extended Reality for Urban Services," IEEE Access, vol. 11, pp. 92478-92495, 2023. doi: 10.1109/ACCESS.2023.3307639.

[4] Y. Li et al., "A Deep Learning-Based Hybrid Framework for Object Detection and Recognition in Autonomous Driving," IEEE Access, vol. 8, pp. 194228-194239, 2020. doi: 10.1109/ACCESS.2020.3033289.

[5] Razmjoui, Pouyan, et al. "A blockchain-based mutual authentication method to secure the electric vehicles' TPMS." IEEE Transactions on Industrial Informatics 20.1 (2023): 158-168.

[6] A. Kumar, U. K. Singh, and B. Pradhan, "Enhancing Interpretability in Deep Learning-Based Inversion of 2-D Ground Penetrating Radar Data: An Explainable AI (XAI) Strategy," IEEE Geoscience and Remote Sensing Letters, vol. 21, pp. 1-5, 2024. doi: 10.1109/LGRS.2024.3400934.

[7] Fard, Abdollah Kavousi, et al. "Superconducting fault current limiter allocation in reconfigurable smart grids." In 2019 3rd International Conference on Smart Grid and Smart Cities (ICSGSC), pp. 76-80. IEEE, 2019.

[8] Esapour, Khodakhast, et al. "A novel energy management framework incorporating multi-carrier energy hub for smart city." IET Generation, Transmission & Distribution 17, no. 3 (2023): 655-666.

[9] W. Huang et al., "Collaborating Ray Tracing and AI Model for AUV-Assisted 3-D Underwater Sound-Speed Inversion," IEEE Journal of Oceanic Engineering, vol. 46, no. 4, pp. 1372-1390, Oct. 2021. doi: 10.1109/JOE.2021.3066780.

[10] J. Dai, R. Ma and H. Ai, "Semi-automatic Extraction of Rural Roads From High-Resolution Remote Sensing Images Based on a Multifeature Combination," IEEE Geoscience and Remote Sensing Letters, vol. 19, pp. 1-5, 2022. doi: 10.1109/LGRS.2020.3026674.

[11] Feng, Cong, et al. "Advanced machine learning applications to modern power systems." In New Technologies for Power System Operation and Analysis, pp. 209-257. Academic Press, 2021.

[12] Ferdowsi, Farzad, et al. "Optimal scheduling of reconfigurable hybrid AC/DC microgrid under DLR security constraint." In 2019 IEEE Green Technologies Conference (GreenTech), pp. 1-5. IEEE, 2019.

[13] D. A. Vega-Oliveros and O. Koren, "Measuring Spatiotemporal Civil War Dimensions Using Community-Based Dynamic Network Representation (CoDNet)," IEEE Transactions on Computational Social Systems, vol. 11, no. 1, pp. 1506-1516, Feb. 2024. doi: 10.1109/TCSS.2023.3241173.

[14] Kavousi-Fard, Abdollah, et al. "Digital Twin for mitigating solar energy resources challenges: A Perspective Review." Solar Energy 274 (2024): 112561.

[15] Tajalli, Seyede Zahra, et al. "A secure distributed cloud-fog based framework for economic operation of microgrids." In 2019 IEEE Texas Power and Energy Conference (TPEC), pp. 1-6. IEEE, 2019.

[16] Taherzadeh, Erfan, et al. "New optimal power management strategy for series plug-in hybrid electric vehicles." International Journal of Automotive Technology 19 (2018): 1061-1069.

[17] Dabbaghjamanesh, Morteza, et al. "A new efficient stochastic energy management technique for interconnected AC microgrids." In 2018 IEEE Power & Energy Society General Meeting (PESGM), pp. 1-5. IEEE, 2018.

[18] Moeini, Amirhossein, et al. "Artificial neural networks for asymmetric selective harmonic current mitigation-PWM in active power filters to meet power quality standards." IEEE Transactions on Industry Applications (2020).

[19] Wang, Boyu, et al. "AI-enhanced multi-stage learning-to-learning approach for secure smart cities load management in IoT networks." Ad Hoc Networks 164 (2024): 103628.

[20] Dabbaghjamanesh, Morteza, et al. "Networked microgrid security and privacy enhancement by the blockchain-enabled Internet of Things approach." In 2019 IEEE Green Technologies Conference (GreenTech), pp. 1-5. IEEE, 2019.

[21] D. V. Kute et al., "Deep Learning and Explainable Artificial Intelligence Techniques Applied for Detecting Money Laundering–A Critical Review," IEEE Access, vol. 9, pp. 82300-82317, 2021. doi: 10.1109/ACCESS.2021.3086230.

[22] D. Nguyen et al., "GeoTrackNet—A Maritime Anomaly Detector Using Probabilistic Neural Network Representation of AIS Tracks and A Contrario Detection," IEEE Transactions on Intelligent Transportation Systems, vol. 23, no. 6, pp. 5655-5667, June 2022. doi: 10.1109/TITS.2021.3055614.

[23] Wang, Boyu, et al. "Cybersecurity enhancement of power trading within the networked microgrids based on blockchain and directed acyclic graph approach." IEEE Transactions on Industry Applications 55, no. 6 (2019): 7300-7309.

[24] Tahmasebi, Dorna, et al. "A security-preserving framework for sustainable distributed energy transition: Case of smart city." Renewable Energy Focus 51 (2024): 100631.

[25] Jafari, Mina, et al. "A survey on deep learning role in distribution automation system: a new collaborative Learning-to-Learning (L2L) concept." IEEE Access 10 (2022): 81220-81238.

[26] Khazaei, Peyman, et al. "Applying the modified TLBO algorithm to solve the unit commitment problem." In 2016 World Automation Congress (WAC), pp. 1-6. IEEE, 2016.

[27] Dabbaghjamanesh, Morteza, et al. "High performance control of grid connected cascaded H-Bridge active rectifier based on type II-fuzzy logic controller with low frequency modulation technique." International Journal of Electrical and Computer Engineering 6, no. 2 (2016): 484.

[28] Khazaei, Peyman, et al. "A high efficiency DC/DC boost converter for photovoltaic applications." International Journal of Soft Computing and Engineering (IJSCE) 6, no. 2 (2016): 2231-2307.

[29] S. Kolekar et al., "Behavior Prediction of Traffic Actors for Intelligent Vehicle Using Artificial Intelligence Techniques: A Review," IEEE Access, vol. 9, pp. 135034-135058, 2021. doi: 10.1109/ACCESS.2021.3116303.

[30] Q. Xiao et al., "The long-term trend of PM2.5-related mortality in China: The effects of source data selection," Chemosphere, vol. 263, Article 127894, 2021.

[31] Mohammadi, Mojtaba, et al. "Effective management of energy internet in renewable hybrid microgrids: A secured data driven resilient architecture." IEEE Transactions on Industrial Informatics 18, no. 3 (2021): 1896-1904.

[32] Dabbaghjamanesh, Morteza, et al. "A novel distributed cloud-fog based framework for energy management of networked microgrids." IEEE Transactions on Power Systems 35, no. 4 (2020): 2847-2862.

[33] E. Luo et al., "Urban poverty maps-From characterising deprivation using geo-spatial data to capturing deprivation from space," Sustain. Cities Soc., vol. 84, Article 104033, 2022.

[34] Ashkaboosi, Maryam, et al. "An optimization technique based on profit of investment and market clearing in wind power systems." American Journal of Electrical and Electronic Engineering 4, no. 3 (2016): 85-91.

[35] Dabbaghjamanesh, Morteza, et al. "Deep learning-based real-time switching of hybrid AC/DC transmission networks." IEEE Transactions on Smart Grid 12, no. 3 (2020): 2331-2342.

[36] Dabbaghjamanesh, Morteza, et al. "Stochastic modeling and integration of plug-in hybrid electric vehicles in reconfigurable microgrids with deep learning-based forecasting." IEEE Transactions on Intelligent Transportation Systems 22, no. 7 (2020): 4394-4403.

[37] A. Rossi et al., "Modelling taxi drivers' behaviour for the next destination prediction," IEEE Transactions on Intelligent Transportation Systems, vol. 21, pp. 2980-2989, 2019.

[38] O. Suissa et al., "Toward a Period-specific optimized neural network for OCR error correction of historical Hebrew texts," ACM J. Comput. Cultural Heritage (JOCCH), vol. 15, pp. 1-20, 2022.

[39] Kavousi-Fard, Abdollah, et al. "IoT-based data-driven fault allocation in microgrids using advanced µPMUs." Ad Hoc Networks 119 (2021): 102520.

[40] Kazemi, Behzad, et al. "IoT-enabled operation of multi energy hubs considering electric vehicles and demand response." IEEE Transactions on Intelligent Transportation Systems 24, no. 2 (2022): 2668-2676.

[41] Razmjouei, Pouyan, et al. "DAG-based smart contract for dynamic 6G wireless EVs charging system." IEEE Transactions on Green Communications and Networking 6, no. 3 (2022): 1459-1467.

[42] Mohammadi, Hossein, et al. "Ai-based optimal scheduling of renewable ac microgrids with bidirectional lstm-based wind power forecasting." arXiv preprint arXiv:2208.04156 (2022).

[43] Tajalli, Seyede Zahra, et al. "DoS-resilient distributed optimal scheduling in a fog supporting IIoT-based smart microgrid." IEEE Transactions on Industry Applications 56, no. 3 (2020): 2968-2977.

[44] X. Qin et al., "What makes better village economic development in traditional agricultural areas of China? Evidence from 338 villages," Habitat Int., vol. 106, Article 102286, 2020.

[45] Y. Zhou et al., "Using multi-task learning and deep reinforcement learning to support low-carbon transportation in smart cities," Sustain. Cities Soc., vol. 88, Article 104399, 2023.

[46] J. Monteiro et al., "Spatial disaggregation of historical census data leveraging multiple sources of ancillary information," ISPRS Int. J. Geo Inf., vol. 8, p. 327, 2019.

[47] Dabbaghjamanesh, Morteza, et al. "A novel two-stage multi-layer constrained spectral clustering strategy for intentional islanding of power grids." IEEE Transactions on Power Delivery 35, no. 2 (2019): 560-570.

[48] Kavousi-Fard, Abdollah, et al. "An evolutionary deep learning-based anomaly detection model for securing vehicles." IEEE Transactions on Intelligent Transportation Systems 22, no. 7 (2020): 4478-4486.